Journal of Magnetism and Magnetic Materials 358-359 (2014) 105–118

Contents lists available at ScienceDirect

Journal of Magnetism and Magnetic Materials

journal homepage: www.elsevier.com/locate/jmmm

Kinetic modeling of thermal decomposition of zinc ferrite from neutral leach residues based on stochastic geometric model

Bojan Janković [a,*], Srećko Stopić [b], Aybars Güven [b], Bernd Friedrich [b]

[a] Faculty of Physical Chemistry, Department for Dynamics and Matter Structure, University of Belgrade, Studentski trg 12-16, P.O. Box 137, 11001 Belgrade, Serbia
[b] IME Process Metallurgy and Metal Recycling, RWTH Aachen University, Aachen, Germany

ARTICLE INFO

Article history:
Received 4 June 2013
Received in revised form
20 January 2014
Available online 31 January 2014

Keywords:
Kinetic modeling
Zinc ferrite
X-ray diffraction
Geometric model
Autocatalytic stage
Thermodynamic property

ABSTRACT

The stochastic geometric model was applied to kinetic modeling the complex process of thermal decomposition of zinc ferrite from neutral leach residues, at different operating temperatures (600 °C, 750 °C, 950 °C and 1150 °C). Based on functional dependence of Avrami's constant (n) in a function of the effective activation energy (E_a), it was found that at $T > 950$ °C, the crystallization process takes place in autocatalytic stage, under the conditions where the rate of nucleation rapidly increases. It was established that the high nucleation rate can be attributed to formation of both Zn and Fe rich regions which provide a high number of heterogeneous nucleation sites. Based on the obtained final shape of the particles, it was found a strong presence of zinc, iron (present only in the form of Fe_3O_4 (magnetite)), magnesium (in the form of $Mg_2Si_2O_6$), and also lead oxides. Thermodynamic analysis showed that the decomposition depends on the introduction of heat, and exerts a positive value of the Gibbs free energy of activation. Such a feature was expected since the ferrite system has been submitted to a forced decomposition and volatilization reactions.

1. Introduction

Zinc is an important element especially for the steel industry and the formation of Electric Arc Furnace Dust (EAFD) leads to strong recycling activities. Zinc in primary fluidized bed calcine as well as in EAFD exists besides as simple oxides in a spinel form called zinc ferrite $ZnO \cdot Fe_2O_3$. A lot of studies have been conducted to find the most efficient way of zinc and iron recovery from the EAFD material due to environmental, technical and economical needs. Because of that there is a necessity for treatment of wastes containing zinc ferrites [1,2]. Different hydrometallurgical ways for recovering zinc from ferrite-phases exist such as acidic or caustic leaching, microwave assisted extraction, EZINEX process, etc. [3–5].

Leaching with sulfuric acid to obtain high recovery yield is feasible based on the following reaction:

$$ZnFe_2O_4 + 4H_2SO_{4\,(aq)} \rightarrow ZnSO_{4\,(aq)} + Fe_2(SO_4)_3 + 4H_2O. \quad (1)$$

Eq. (1) can be expected even at room temperature, but the reaction rate is too slow. At the elevated temperatures and longer leaching time, significant extraction yields $> 80\%$ will occur, but the process is un-selectively decreased [6]. Zinc extraction becomes even higher if the solid/acid ratio is lowered. During this process, calcium sulfate precipitates resulting from low concentration of sulfuric acid and it remains until the end of process. Because of unselective leaching a yield of zinc is decreased [6]:

$$ZnFe_2O_4 + 2[OH^-] \rightarrow ZnO_2^{2-} + Fe_2O_3 + H_2O. \quad (2)$$

Other researches [5] have studied leaching kinetics of zinc ferrite in aqueous hydrochloric acid solutions according to reaction (3) and found that it is possible to precipitate ferric chloride, in the pH range of 3–4 and using air mixing:

$$ZnFe_2O_4 + 2HCl \rightarrow ZnCl_2 + Fe_2O_3 + H_2O \quad (3)$$

Their experiments have reached up to 90% zinc recovery under pH values between 3 and 4 at 90 °C. Unsuccessful experiments on ammonia leaching were conducted, where the EAF dust was firstly washed to solubilize the zinc oxide and then leached with ammonium chloride. But the zinc ferrite remains in residue. An organic acid process was also able to recover zinc from ferrite, when additional leaching step was introduced [5].

Today's commercial operations reach almost complete winning of zinc from zinc ferrite mostly are based on fuming operations that reduces ferrite and vaporizes zinc. Such pyrometallurgical applications use a reduction media such as carbon monoxide, hydrogen or coke [7].

* Corresponding author. Tel./fax: +381 112187133.
E-mail address: bojanjan@ffh.bg.ac.rs (B. Janković).

0304-8853/$ - see front matter © 2014 Elsevier B.V. All rights reserved.
http://dx.doi.org/10.1016/j.jmmm.2014.01.046

The carbothermic method [8] requires a minimum temperature of 800 °C and the partial pressure of zinc vapor which remains below 0.014 bar. A full reduction of EAF dust with hydrogen at lower temperatures produces both iron and zinc with double hydrogen requirement, compared to the selective reduction that only produces zinc [2]. The worldwide standard is thermal reductive treatment in the Waelz process [9] enabling strong destruction of the zinc ferrite whereby producing a slag with very limited probability for use and high energy input [10].

1.1. The main objective of the presented investigation

In last five years, the process development for high pressure and atmospheric leaching of electric arc furnace dust became a central part of research at the IME, RWTH Aachen University in Germany. For example, high pressure leaching revealed to be more effective from zinc extraction point of view, but not for iron [11]. Unfortunately, it was found that the high selectivity is obtained only with lower a/d ratios. In order to decompose zinc ferrite from neutral leach residues, a new experimental concept was developed and conceptually presented in Ref. [1].

In this paper, we present a theoretical concept to explain the detailed reaction mechanism of the isothermal decomposition of zinc ferrite from neutral leach residues, which, in itself, is a very complex physico-chemical process. The procedure was based on explanation of the process from the standpoint of the theory of the nucleation and growth of a new phase, presented as the stochastic geometric model (Johnson–Mehl and Avrami (JMA)) [12–15]. Actually, this approach involves the consideration of the process in the light of solid state phase transformation kinetics [16]. The kinetic consideration was supported by the proper thermodynamic (through the changes of thermodynamic functions) analysis [17]. This approach has an interesting potential for describing the decomposition kinetics of the considered system, when the system is subjected to the elevated temperatures under controlled experimental conditions. Mathematical modeling of such complex decomposition can be of crucial importance for the design, performance analysis, and further improvement of hydrometallurgical processes, which, as one of the major products provide separation of specific magnetic materials. This is very significant since that at the elevated operating temperature (above 1025 °C), solid solutions of both ferric and zinc oxides in zinc ferrite can be formed, and that, when heated to higher operating temperatures the dissolved ferric oxide lost oxygen, forming magnetite and the specimen became ferromagnetic. One of the main goals of the current investigation is to identify the factors affecting the kinetics of the overall decomposition process, where, as one of the products can expect the appearance of iron, in the form of magnetite.

2. Experimental

2.1. Material characterization

The zinc leach residue was obtained from former company Ruhr-Zink, Datteln, Germany, with a moisture content of 23%. Before the experimental investigation, the sample was dried at 120 °C overnight in order to eliminate the moisture presence. The Rietveld XRD (X-ray diffraction) analysis of an initial sample has shown the following chemical composition [in %]: 40.9 $ZnFe_2O_4$, 16.5 $CaSO_4$, 6.4 $MgSO_4$, 13.6 Zn_2SiO_4, 11.3 $PbSO_4$, 4.4 $KFe_3(SO_4)_2(OH)_6$, and 6.9 related to the other compounds. This phase change made materials more soluble and suitable for the leaching process, which was reported in our previously paper [1]. The gaseous phases of PbO and SO_2 were formed during thermal decomposition and removed with nitrogen as the carrier gas. At 1150 °C, the chemical composition of the final decomposed material amounted [in %]: 57.0 Fe_3O_4, 28.9 $Ca_2ZnSi_2O_7$, 8.4 ZnO, 5.0 Mg_2SiO_6 and 0.7 $ZnAl_2O_4$. A scanning electron microscope (model ZEISS DSM 982 Gemini) (SEM) was used for the characterization of the obtained particles. SEM images were used to study the surface morphology. For explanation the thermo-chemical prediction of the formed products, the FactSage® thermochemical software with databases [18] was used.

2.2. The isothermal measurements

After 15 min of heating the samples in order to eliminate the contained moisture, these were used in the thermal treatment experiments performed in the tube furnace. At the fixed operating temperatures (600, 750, 950, 1150 °C), four experiments were performed at each operating temperature in the certain time intervals (15, 20, 25, 30, 35, 40, 45, 50, 55 and 60 min). The experiments were repeated three times. After reaching the aimed temperature, 1 g of the zinc leach residue was inserted in a tubular furnace, under a constant nitrogen gas, with a flow rate of $\varphi = 1\ \mathrm{L\ min^{-1}}$. After beginning of the thermal treatment of dried sample at the fixed operating temperature, the reaction time was measured by chronometer (in digits form). After that, the specimen was taken out from the furnace and placed in the exiccator. The weight results were noted as an average mass lost of the specimen, in order to calculate the decomposition rate.

The conversion fraction (α) in the isothermal measurement at the considered operating temperature T is calculated by the following equation:

$$\alpha = \frac{m_{o(15)} - m_t}{m_{o(15)} - m_f} \tag{4}$$

where $m_{o(15)}$ is the initial mass of the sample (for time at $t = 15$ min, after removing of any remaining moisture at a given temperature (the time period from $t = 0$ min to $t = 15$ min at each of the considered operating temperature T, corresponds to time scale where the removal was done for possible residual moisture)), m_t is the mass of the sample at time t, and m_f is the final constant mass of the sample, after the establishment of the saturation (the saturation involves reaching the conversion value of $\alpha = 1.00$). Thus, the conversion data are calculated for completely dry samples at each of the observed temperatures. The decomposition of zinc leach residue in an inert atmosphere at every considered operating temperature begins after the 15th minute.

3. Theoretical background

Most solid state transformations do not occur instantaneously because obstacles impede the course of the reaction and make it dependent on time. For example, since most transformations involve the formation of at least one new phase that has a composition and/or crystal structure different from that of the parent one's, some atomic rearrangements via diffusion are required. A second impediment to the formation of a new phase is the increase in energy associated with the phase boundaries that are created between parent and product phases. From a microstructural standpoint, the first process to accompany a phase transformation is nucleation – the formation of very small (often submicroscopic) particles, or nuclei, of the new phase, which are capable of growing. Favorable positions for the formation of these nuclei are imperfection sites, especially grain boundaries. The second stage is growth, in which the nuclei increase in size. During this process, some volume of the parent phase disappears. The transformation reaches completion if growth of these new phase

particles is allowed to proceed until the equilibrium fraction is attained.

As would be expected, the time dependence of the transformation rate (which is often termed the kinetics of a transformation) is an important consideration in the heat treatment of materials. With many kinetic investigations, the fraction of reaction that has occurred is measured as a function of time, while the temperature is maintained constant. Data are plotted as the fraction of transformed material (α) versus the time (t) (the kinetic conversion curves). The obtained curves represent the typical kinetic behavior for the most solid-state reactions. For special cases of nucleation and growth, it is possible to derive the analytical description of transformation kinetics according to Johnson–Mehl–Avrami (JMA) stochastic geometric model [12–15]. For solid-state transformations displaying the kinetic behavior through α–t curves, the fraction of transformation (α) is a function of time (t) as follows:

$$\alpha = 1 - \exp\lfloor -(K_A t)^n \rfloor, \tag{5}$$

where K_A and n represent the Avrami rate constant, and the Avrami constant (or the JMA exponent), respectively. Eq. (5) is often referred to as the Avrami equation [13–15]. Usually, the Avrami rate constant K_A is written in the form of the composite Avrami rate constant k_A (i.e. $k_A = K_A^n$). It was shown that k_A (the dimension of which is given in $(\text{time})^{-n}$) is not only a function of temperature, but also a function of the Avrami constant, n [19]. As a result, use of K_A should be more preferable than use of k_A, due to partly to the facts that it is independent of the Avrami constant n and its dimension is given in $(\text{time})^{-1}$. It should be noted that both k_A (and hence K_A) and n are constants specific to a given crystalline morphology and type of nucleation for a particular crystallization condition [20] and that, based on the original assumptions of the theory, the value of the Avrami constant n should be an integer, ranging from 1 to 4. The value of K_A and n can be obtained from the linear relationship as $\ln[-\ln(1-\alpha)] = n \ln K_A + n \ln t$ [13]. By plotting $\ln[-\ln(1-\alpha)]$ against $\ln t$ for different operating temperatures, the JMA plots can be evaluated, in the case of α range ($\Delta\alpha$) where there is a linearity of the data used.

The Avrami rate constant (K_A) can be presented in the form of the Arrhenius equation as:

$$K_A = {k_A}^{1/n} = k_o \exp\left(-\frac{E_a}{RT}\right) \tag{6}$$

where k_o represents the pre-exponential factor [time^{-1}], E_a is the *apparent* or the *effective* activation energy [J mol^{-1}], R is the gas constant [$\text{J K}^{-1}\ \text{mol}^{-1}$], and T is the absolute temperature [K]. Temperature is one variable in a heat treatment process that is subject to control, and it may have a profound influence on the kinetics and thus on the rate of the transformation. For most solid state reactions, and over specific temperature ranges, the rate increases with temperature according to Eq. (6). Processes that exhibit the temperature dependence of the rates through the relationship presented by Eq. (6) are sometimes termed as the thermally activated. The rate of the process expressed through Eq. (5), can be obtained by differentiating Eq. (5) with respect to time (t) and after rearranging of some terms, we can finally get the expression of the form:

$$\frac{d\alpha}{dt} = K_A f(\alpha) = K_A n(1-\alpha)[-\ln(1-\alpha)]^{(n-1)/n}$$
$$\equiv {k_A}^{1/n} n(1-\alpha)[-\ln(1-\alpha)]^{(n-1)/n} \tag{7}$$

where $f(\alpha)$ is the differential form of the function of reaction mechanism. The rate of the process expressed by the differential kinetic equation (Eq. (7)) can be rearranged and integrated as:

$$\int_0^\alpha \frac{d\alpha}{f(\alpha)} \equiv g(\alpha) = [-\ln(1-\alpha)]^{1/n} = K_A t = {k_A}^{1/n} t. \tag{8}$$

In Eq. (8), the $g(\alpha)$ is the integral form of the function of reaction mechanism. By plotting linearly $g(\alpha)$ for several conversion grade α observed experimentally, it is possible to obtain K_A for each operating temperature, which represents the slope of the linear adjustment of $g(\alpha)$ against time (t). The plot of calculated $\ln K_A$ [$\equiv (1/n) \ln k_A$] against $1/T$ according to the Arrhenius postulate (as $\ln K_A = (1/n) \ln k_A = \ln(k_o) - E_a/RT$) allow to deduce the apparent activation energy (E_a) and the pre-exponential factor (k_o).

In the case of continuous nucleation, the *nucleation rate* function $I(t)$ (for quantifying the nucleation rate I as a function of time throughout the course of crystallization) can be introduced as [21]:

$$I(t) = I_c(1+m)t^m, \tag{9}$$

where I_c is the nucleation rate constant (a temperature-dependent, but the time-independent parameter, the dimension of which is given in (number of nuclei/(s^{m+1}, cm^3)), and m represents the *nucleation index*. In the considered case, the Avrami constant can be presented in a more specific mathematical definition as:

$$n = d + m + 1, \tag{9a}$$

where d represents the geometric or *dimensionality index* (e.g. $d=1$ for rod, $d=2$ for disc, and $d=3$ for sphere). According to Eq. (9a), the traditional sense of the Avrami constant n in describing the dimensionality of the crystal geometry is restored with the geometric or dimensionality index d, but, more importantly, abnormality in the experimental observation of the Avrami constant n (viz. fractional values of n, or the values of n greater than 4) can now be theoretically explainable by the introduction of the *nucleation index* m. The qualitative description of the *nucleation index* m (for a fixed value of the geometric index d) in describing the nucleation mechanism throughout the course of the crystallization process can be described in a few significant items:

(a) $m=-1$: *Nucleation mechanism*: instantaneous; *Nature of the nucleation rate over crystallization time*: constant,
(b) $-1<m<0$: *Nucleation mechanism*: instantaneous and sporadic; *Nature of the nucleation rate over crystallization time*: gradually decreasing with time and approaching a constant value at a certain time,
(c) $m=0$: *Nucleation mechanism*: sporadic; *Nature of the nucleation rate over crystallization time*: steadily increasing with time,
(d) $0<m<1$: *Nucleation mechanism*: sporadic; *Nature of the nucleation rate over crystallization time*: increasing with time,
(e) $m>1$: *Nucleation mechanism*: sporadic; *Nature of the nucleation rate over crystallization time*: increasing strongly with time.

Strictly speaking, the JMA kinetic parameters (n, k_o and E_a) can only have certain values, pertaining to specific growth and nucleation models [22]. Mixtures of the specific nucleation models are not considered in the original derivation of JMA kinetics. However, it can be proven (by numerical procedure) for such mixtures of nucleation models that, although the JMA description does not hold exactly, a very good approximation to the observed kinetics can still be given by the JMA description according to Eqs. (5) and (6) [22]. Thus, also intermediate values of the JMA kinetic parameters then are possible. Determined values for the *effective* kinetic parameters can then be interpreted in terms of the basic nucleation and growth models, recognizing the interdependence of the JMA kinetic parameters. It has been shown that the *apparent* (*effective*) activation energy is given by the following

weighted average of the *activation energies* of the involved nucleation and growth processes as [22]:

$$E_a = \frac{(n-1)E_G + E_N}{n} = \frac{(d+m)E_G + E_N}{(d+m+1)},, \tag{10}$$

where E_G and E_N represent the activation energies for the growth and nucleation. If E_a can be measured as function of n (by the variation of the nucleation index through the numerical procedure), in that case Eq. (10) allows us to determine the corresponding values of E_G and E_N, separately.

The apparent (*effective*) activation energy values (E_a) can be calculated at the different and constant values of conversion fraction (or the fraction of transformation) (α), combining Eqs. (6) and (8), and presenting them in logarithmic form, so that we get [23]:

$$-\ln t_{\alpha_{k,i}} = \ln\left[\frac{(k_o)_{\alpha_{k,i}}}{g(\alpha_{k,i})}\right] - \frac{E_{a,\,\alpha_{k,i}}}{RT_i}. \tag{11}$$

Using data at which in different operating temperature runs (T_i) the same value $\alpha = \alpha_{k,i} = \text{const.}$ was reached, the linear relationship $-\ln t_{\alpha k,i}$ versus $1/T_i$ with a slope proportional to $E_{a,\alpha k,i}$ could be established. This method provides a check of invariance of E_a with respect to conversion fraction, α.

The local Avrami constant (n_{loc}) is employed to have the derivative of the Avrami plot against the fraction of transformation, which efficiently gives the local value of n with α [24]. The local Avrami constant is deduced by:

$$n_{loc} \equiv n(\alpha) = \frac{\partial \ln\{\ln[1/(1-\alpha)]\}}{\partial \ln(t)}. \tag{12}$$

The value of local Avrami constant ($n(\alpha)$) gives information about the nucleation and growth behavior, when the crystallized volume fraction is α.

Once the generalized Avrami constant is known (as described above), we can then calculate the Avrami rate constant K_A from half-time analysis [25]. The half-time ($t_{0.50}$) is defined as the time required to achieving 50% of the maximum conversion during the isothermal experiment [25]. The Avrami rate constant (K_A) can be calculated directly from the reciprocal half-time ($t_{0.50}^{-1}$) according to the following equation [25,26]:

$$K_A = (\ln 2)^{1/n} t_{0.50}^{-1}. \tag{13}$$

For the mechanism in which the Avrami constant $n > 1.00$, the rate approaches zero at the beginning of the process (i.e. $t \to 0$), and when the process nears completion (i.e. $t \to \infty$). The maximum rate of the isothermal transformation occurs at time t_{max}, which corresponds to the inflection point of the α versus t curve, where the second derivative of $\alpha(t;T)$ vanishes. Therefore, the t_{max} can be calculated from the following equation [25,27]:

$$t_{max} = \left[\frac{(n-1)}{nk_A}\right]^{1/n}. \tag{14}$$

Since the half-time measurements provide a route to calculate K_A (as well as the composite Avrami rate constant, k_A), the relation that connects t_{max} and $t_{0.50}$ can be expressed in the form [25]:

$$t_{max} = \left[\frac{(n-1)}{n\ln 2}\right]^{1/n} t_{0.50}. \tag{15}$$

The ratio $t_{max}/t_{0.50}$ allows us to compare the differences between $t_{0.50}$ and t_{max} if they exist, for a given value of the Avrami constant (n), evaluated at the considered operating temperature.

One of the frequently applied test to verify the applicability of the JMA mechanism is based on the properties of two special functions, which are labeled as $Y(\alpha)$ and $Z(\alpha)$ functions [28,29]. In isothermal conditions, however, the magnitude K_A (expressed through Eq. (6)) in Eq. (7) is constant and the rate of the process ($d\alpha/dt$) is approximately equal to $f(\alpha)$ function, as:

$$Y(\alpha) = \left(\frac{d\alpha}{dt}\right) \approx f(\alpha) \tag{16}$$

If the rate of the process at considered operating temperature is plotted as a function of α its shape corresponds to the $f(\alpha)$ function. It is convenient to normalize the $Y(\alpha)$ plot within [0,1] interval. Combining Eqs. (7) and (8), the other function $Z(\alpha)$ can be defined as:

$$Z(\alpha) = \left(\frac{d\alpha}{dt}\right) t = f(\alpha)g(\alpha) \tag{17}$$

For practical reasons this function is normalized within [0,1] interval. The $Y(\alpha)$ and $Z(\alpha)$ functions exhibit maxima at α_m and α_p^{∞}, respectively. The maximum of the $Y(\alpha)$ function for the JMA mechanism depends on the value of the Avrami constant:

$$\alpha_m = 1 - \exp\left[\frac{(1-n)}{n}\right], \text{ for } n > 1.00 \tag{18}$$

and

$$\alpha_m = 0 \text{ for } n \le 1.00. \tag{18a}$$

The value of α_m is always lower than the maximum of the $Z(\alpha)$ function, α_p^{∞}. The latter is a constant in the case of the JMA mechanism, where we have:

$$\alpha_p^{\infty} = 0.632. \tag{18b}$$

The value of α_p^{∞} in Eq. (18b) is the characteristic "fingerprint" of the JMA reaction mechanism. This procedure can be used as the simple test of the applicability of JMA theory of nucleation and growth kinetics, in the case of the investigated decomposition process.

In addition, if the $Y(\alpha)$ function has a maximum in the interval between 0 and α_p (where α_p represents the conversion fraction, which corresponds to the maximum value of the differential rate conversion curves, presented as $d\alpha/dt$ against t) i.e., for $n > 1.00$, then the Avrami constant (n) can be calculated from Eq. (18), but now re-written in a somewhat different mathematical form, as [28]:

$$n = \frac{1}{1 + \ln(1-\alpha_m)}. \tag{19}$$

3.1. Thermodynamic considerations

Based on the optimized values of the apparent (*effective*) activation energy and the pre-exponential factor, using the appropriate selected reaction model function, the values of thermodynamic functions ($\Delta S^{\neq}$, $\Delta H^{\neq}$ and $\Delta G^{\neq}$) can be calculated. The pre-exponential factor (k_o) can be estimated from the intercept of the plots of Eq. (11), by inserting the most probable determined $g(\alpha)$ function.

The change of the entropy of activation ($\Delta S^{\neq}$) may be calculated according to the Eq. (20) [30]:

$$\Delta S^{\neq} = R \ln\left(\frac{k_o h}{e\chi k_B T}\right) \tag{20}$$

where k_o is the pre-exponential factor, $e = 2.7183$ is the Neper number, χ is the transmission coefficient, which is unity for monomolecular reactions, k_B is the Boltzmann constant (1.381×10^{-23} J K^{-1}), h is the Planck's constant (6.626×10^{-34} J s), R is the universal gas constant (8.314 J K^{-1} mol^{-1}) and T represents the considered value of the operating temperature (K).

The change of the enthalpy of activation ($\Delta H^{\neq}$) may be obtained according to Eq. (21) [30]:

$$\Delta H^{\neq} = E^{\neq} - RT \tag{21}$$

where $E^{\neq}$ is the apparent activation energy, E_a, obtained from the iterative procedure of Eq. (11).

The change of the Gibbs free energy of activation ($\Delta G^{\neq}$) for the investigated decomposition process, can be calculated using the well-known thermodynamic equation, in the form [30,31]:

$$\Delta G^{\neq} = \Delta H^{\neq} - T\Delta S^{\neq} \tag{22}$$

4. Results

4.1. Experimental conversion curves

The experimentally obtained isothermal conversion (α–t) curves for the decomposition process of zinc ferrite from neutral leach residues, at the operating temperatures of 600 °C, 750 °C, 950 °C and 1150 °C in an inert atmosphere are presented in Fig. 1.

The rate of decomposition increases with an increase in operating temperature, and at T=1150 °C, approximately 100% is achieved in less than 35 min. In that case, the decomposition process of zinc ferrite from neutral leach residues should be performed at the operating temperatures $T \geq 600$ °C to investigate the whole decomposition process, within a reasonable reaction time period.

4.2. Isoconversional $E_a = E_a(\alpha)$ dependence

The fundamental assumption of the isothermal isoconversional methods is that a single rate equation is applicable only to a single extent of conversion and to the time region (Δt) related to this conversion. In other words, the isoconversional methods describe the kinetics of the process by using the multiple single rate (or single-step) kinetic equations, each of which is associated with a certain extent of conversion. With regard to this advantage, the isoconversional methods allow complex (i.e., multi-step) processes to be detected *via* a variation of the apparent (*effective*) activation energy (E_a) with a conversion, α. Conversely, independence of E_a on α is a sign of a single-step process. The apparent activation energy–conversion correlation, usually corresponds to the change of the reaction mechanisms; it may reflect relative contributions of the parallel reaction channels to the overall kinetics of the process.

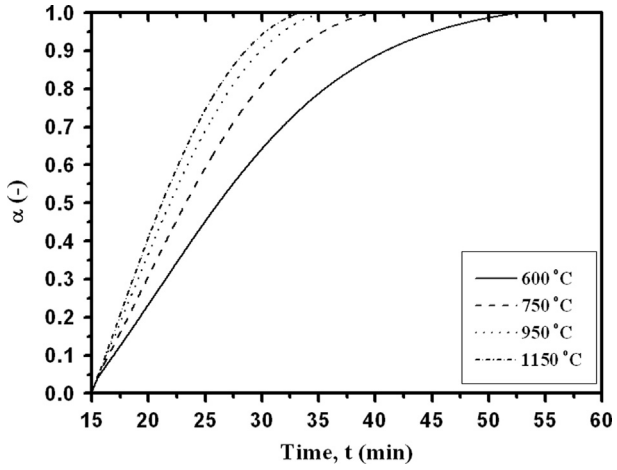

Fig. 1. The experimentally obtained conversion (α–t) curves for the isothermal decomposition process of zinc ferrite from neutral leach residues, at the different operating temperatures (T=600 °C, 750 °C, 950 °C and 1150 °C) in an inert atmosphere (the experimental curves are presented in a *B*-spline graphic configuration modes).

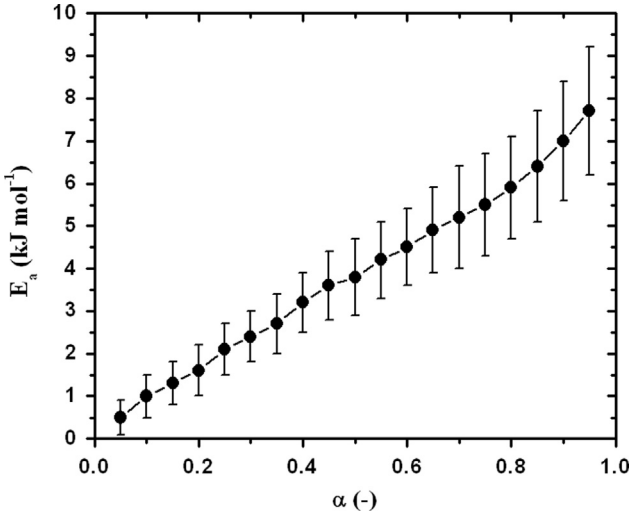

Fig. 2. The dependence of the apparent (*effective*) activation energy (E_a) on the fraction of transformation (α), evaluated by application of Eq. (11), for the isothermal decomposition process of zinc ferrite from neutral leach residues. The errors in calculated E_a values are presented by the error bars.

Fig. 2 shows the dependence of E_a on α evaluated by application of Eq. (11), for the considered decomposition process of zinc ferrite from neutral leach residues. The corresponding relative error values of E_a are given by the error bars (Fig. 2).

As shown in Fig. 2, the dependence $E_a = E_a(\alpha)$ exhibits a progressive increase in E_a values, in the whole range of the considered conversion (α) values ($0.05 \leq \alpha \leq 0.95$). This behavior of E_a values with α is the characteristic for the processes involving parallel competing reactions [32,33].

4.3. Double logarithmic plots analysis

The values of K_A and n were calculated from the linear relationship $\ln[-\ln(1-\alpha)]$ against $\ln t$ at the different operating temperatures. The data for $0.15 \leq \Delta\alpha \leq 0.95$ are almost located on straight lines (not shown). The values of intercepts of the obtained straight lines ($n \ln K_A$), the logarithmic values of K_A ($\ln K_A$), the values of K_A, as well as the values of the Avrami constant (n), are listed in Table 1.

It can be seen from Table 1, that the good linearity ($R^2 > 0.98500$) indicates that it is valid to illustrate the decomposition process by the Avrami equation (Eq. (5)). Also, it can be observed that the values of the Avrami rate constant (K_A) increased as the operating temperature increased, which directly suggests the following facts: the higher operating temperature, the faster the decomposition process, which is in good agreement with the general rule of chemical reactions [34]. As we have known, the Avrami constant provides qualitative information on the nature of the nucleation and the growth processes in the overall crystallization, and may be changed. This fact of change in n (Table 1) may imply that a change occurs in the decomposition mechanism, during the transition from a lower to a very high value area of the operating temperatures.

4.4. Dimensionality and nucleation index results with local Avrami constant behavior

Based on the obtained values of n, the corresponding values of dimensionality and nucleation index were estimated, by application of Eq. (9a). For investigated decomposition process, the values of d and m, together with a qualitative description of crystallization phenomena at the different operating temperatures, are listed in Table 2.

Table 1
Values of $n \ln K_A$, $\ln K_A$, K_A and n calculated from the linear dependence of $\ln[-\ln(1-\alpha)]$ against $\ln t$ at different operating temperatures (T=600, 750, 950, 1150 °C) in considered conversion ranges ($\Delta\alpha$), for the decomposition process of zinc ferrite from neutral leach residues.

Operating temperature, T (°C)	Conversion range, $\Delta\alpha$ (–)	$n \ln K_A$	$\ln K_A$, K_A (min^{-1})	K_A (min^{-1})	n	R^2 [a]
600	0.15–0.95	−10.09495	−3.41046	0.03303	2.96 ± 0.03	0.99165
750	0.15–0.95	−12.32582	−3.26080	0.03836	3.78 ± 0.05	0.99210
950	0.15–0.95	−13.75917	−3.18499	0.04138	4.32 ± 0.07	0.99198
1150	0.15–0.95	−14.94514	−3.15298	0.04272	4.74 ± 0.09	0.98775

[a] Adj. R-square.

Table 2
The dimensionality and nucleation indexes (d and m) with a qualitative description of crystallization phenomena identified for the isothermal decomposition process of zinc ferrite from neutral leach residues, at the operating temperatures of 600 °C, 750 °C, 950 °C and 1150 °C.

Operating temperature, T (°C)	d	m	$d+m$	Nucleation mechanism	The nucleation rate over crystallization time
600	1.96	0	1.96	Sporadic (disc)	Steadily increasing with time
750	3.00	−0.22	2.78	Instantaneous and sporadic (sphere)	Gradually decreasing with time and approaching a constant value
950	3.00	0.32	3.32	Sporadic (sphere)	Increasing with time
1150	3.00	0.74	3.74	Sporadic (sphere)	Increasing with time
Average	2.74	0.21	2.95	Sporadic (sphere)	Increasing with time

Table 3 shows the relationships between E_G and E_N in the *effective* activation energy for the considered decomposition process, at the different operating temperatures (600 °C, 750 °C, 950 °C and 1150 °C). The same table (Table 3) also shows the overall (averaged) relation for the effective activation energy with the corresponding contributions of the activation energies for the growth and nucleation processes, respectively.

Fig. 3 shows the local Avrami constant ($n(\alpha)$) values as a function of α, for the decomposition process of zinc ferrite from neutral leach residues, at the different operating temperatures. The local Avrami constant is not considered for a fraction of transformation lower than 0.05 (5%) or higher than 0.95 (95%) because of large error.

Table 3
The specific relationships between E_G and E_N contributions to the apparent (*effective*) activation energy for the decomposition process of zinc ferrite from neutral leach residues, at the different operating temperatures (T=600 °C, 750 °C, 950 °C and 1150 °C). (The relationships are derived, on the basis of Eq. (10)).

Operating temperature, T (°C)	Effective activation energy for crystallization, E_a (kJ mol^{-1})[a]
600	$(2/3)E_G+(1/3)E_N$
750	$(14/19)E_G+(5/19)E_N$
950	$(10/13)E_G+(3/13)E_N$
1150	$(15/19)E_G+(4/19)E_N$
Average	$(3/4)E_G+(1/4)E_N$

[a] The relationships were most closely calculated, since $(d+m+1)$ are non-integers.

4.5. Functional dependence of the Avrami constant on the effective activation energy

Based on Eq. (10), the values of the Avrami constant n and the effective activation energies can be plotted in one graph as shown in Fig. 4.

The effective activation energy (E_a) for a wide range of d and m modes with Arrhenius temperature dependence can be expressed through Eq. (10). From Fig. 4 we can see that the calculated values of E_a (using Eq. (10)) decreases with the obtained values of n, showing a rising trend. In the variable range of the Avrami constant n, where extends from 2.90 to 4.63, the E_a value decreases up to extremely low value equal to 0.8 kJ mol^{-1}. It can be observed three regions (Regions I, II and III in Fig. 4) with characteristic changes in E_a and n values. The red dot line in Fig. 4 represents the fit curve of the Eq. (10), where the values of E_N and E_G can be calculated. Applying the averaging procedure, the following values were found: $\langle E_N\rangle$=3.9 kJ mol^{-1} and $\langle E_G\rangle$=4.4 kJ mol^{-1}, for the activation energies of the nucleation and growth, respectively.

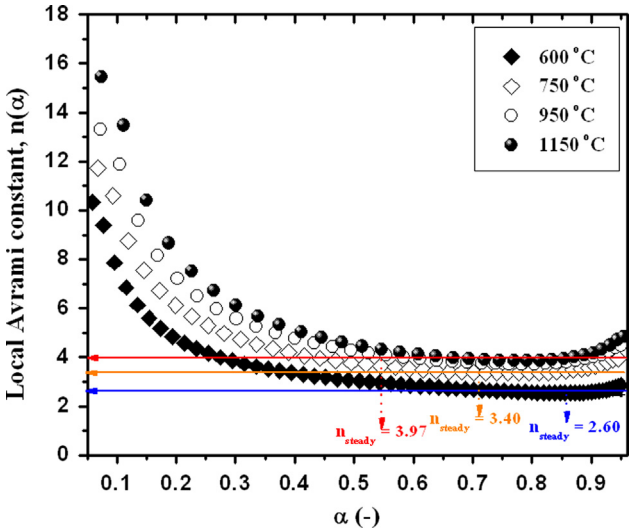

Fig. 3. Relationship between the local Avrami constant ($n(\alpha)$) and the fraction of transformation (α), for the isothermal decomposition process of zinc ferrite from neutral leach residues, at the different operating temperatures (steady state values of the local Avrami constant are designated by n_{steady}). (For interpretation of the references to color in this figure legend, the reader is referred to the web version of this article.)

4.6. Characteristics of special $Y(\alpha)$ and $Z(\alpha)$ functions for the investigated decomposition process

In order to test the validity of JMA theory to explain the decomposition process of zinc ferrite from neutral leach residues, the two special functions, $Y(\alpha)$ and $Z(\alpha)$, were applied. The functions

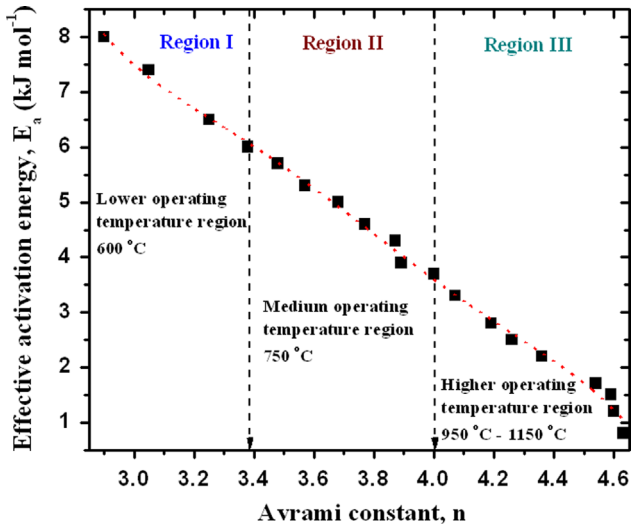

Fig. 4. The effective activation energy (E_a) versus the Avrami constant (n), for the isothermal decomposition process of zinc ferrite from neutral leach residues; the dot red line in the same figure represents the fit curve of Eq. (10), which was calculated using the averaging procedure. The corresponding reaction regions (designated by the different colors as I, II and III) are also presented. (For interpretation of the references to color in this figure legend, the reader is referred to the web version of this article.)

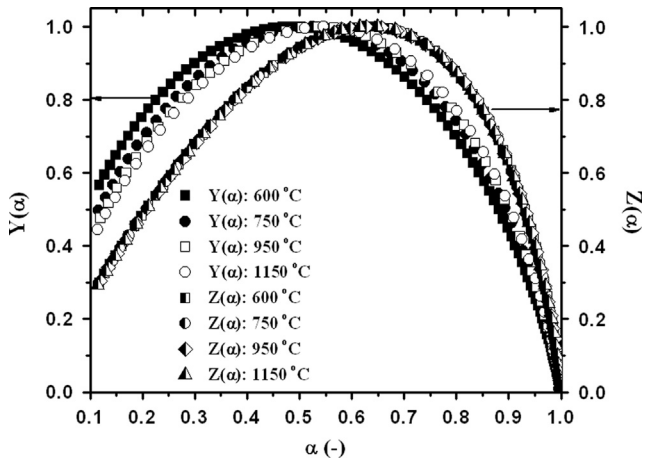

Fig. 5. The normalized $Y(\alpha)$ and $Z(\alpha)$ functions, for the isothermal decomposition process at the different operating temperatures (T=600 °C, 750 °C, 950 °C and 1150 °C).

$Y(\alpha)$ and $Z(\alpha)$ were obtained from the isothermal experimental ($d\alpha/dt$) data, using Eqs. (16) and (17), and they are shown in Fig. 5.

The shape of $Z(\alpha)$ functions are practically invariant with respect to the operating temperature. On the other hand, the shape of $Y(\alpha)$ functions shows the variation with an operating temperature, where the variation is more manifested at the lower values of conversion ($\alpha < 0.45$) (Fig. 5). Since, the $Z(\alpha)$ function does not show the variation with operating temperature, this means that the analytical form of the function of reaction mechanism *does not change in the observed range of the operating temperatures* ($600 \le T \le 1150$ °C) (in the above presented results, we have assumed that the entire decomposition process occurs by the crystallization mechanism in the framework of the JMA theory).

However, the variation of $Y(\alpha)$ function with an operating temperature indicates that the process is not simple, but that the investigated decomposition corresponds to a complicated process (which may includes parallel or consecutive processes). Each of these processes can be characterized by continuous variation in the values of the Avrami constant in different operating temperature regions. This is confirmed by the variation of the local Avrami constant and the effective activation energy values, with a conversion, α.

Table 4
Values of α_m and α_p^{∞} for the normalized $Y(\alpha)$ and $Z(\alpha)$ functions [0,1], as well as the values of the Avrami constant (n) calculated using Eq. (19), for the decomposition process of zinc ferrite from the neutral leach residues, at the different operating temperatures (T=600 °C, 750 °C, 950 °C and 1150 °C); the values of the Avrami rate constant (K_A) calculated by Eq. (8) are also given.

Operating temperature, T (°C)	α_m	α_p^{∞}	n	K_A (min^{-1})[a]
600	0.484	0.638	2.96	0.03303
750	0.521	0.623	3.79	0.03836
950	0.536	0.627	4.31	0.04137
1150	0.546	0.649	4.75	0.04272

[a] Eq. (8).

The maximum of the $Z(\alpha)$ function is located at $\alpha_p^{\infty} \approx 0.632$, and, therefore, the curves in Fig. 5 evidently correspond to the JMA kinetic model. This is confirmed also by the shape of the $Y(\alpha)$ function, which exhibits a maximum (α_m) below α_p^{∞}. Table 4 lists the values of α_m and α_p^{∞} at the different operating temperatures, for the decomposition process of zinc ferrite from neutral leach residues.

From Table 4, we can see that the value of α_m increases with an increasing of the operating temperature, while the values of α_p^{∞} clearly indicate on the presence of the JMA kinetic model to describe the isothermal decomposition process of zinc ferrite from neutral leach residues. The values of the Avrami constant (n) at the different operating temperatures are also calculated, using Eq. (19). These results are also shown in Table 4. It can be observed that the values of the Avrami constant, calculated by Eq. (19), are in excellent agreement with the values of the Avrami constant, presented in Table 1 (which are calculated from the functional dependence of $\ln[-\ln(1-\alpha)]$ against $\ln t$).

4.7. The analytical form of integral function of the reaction mechanism

To check the validity of the obtained values for K_A (Table 1) and the JMA kinetic model with the appropriate values of n, the kinetic method based on Eq. (8) was applied. Fig. 6 shows the linear dependence of $[-\ln(1-\alpha)]^{1/n}$ (which represents the integral form of reaction mechanism function, $g(\alpha)$) against t, for the Avrami constants of n=2.96, 3.78, 4.32 and 4.74 at T=600, 750, 950, and 1150 °C, respectively.

Based on the obtained super-correlations (R^2=1.00000) at all of the observed operating temperatures, from the slopes of the straight lines (Fig. 6), the corresponding values of K_A were calculated. The obtained values for K_A are presented in Table 4. It may be noted that these values (see Table 4) are fully consistent with the values of K_A calculated on the basis of dependency $\ln[-\ln(1-\alpha)]$ against $\ln t$ (Table 1).

From the Arrhenius dependence $\ln(K_A)$ as a function of $1/T$, the corresponding values for the *overall apparent* activation energy (E_a) and the *overall pre-exponential factor* (k_o) can be calculated from the slope and the intercept of the obtained straight line, respectively. For the presentation of the term $\ln(K_A)$, the values of $\ln K_A$ from Table 1 were used. The following values of E_a and k_o were obtained: $E_a = 4.8 \pm 1.9$ kJ mol^{-1} and $k_o = 0.0656$ min^{-1}. The estimated value of E_a corresponds to the approximate value of E_a=4.9 kJ mol^{-1} at α=0.65 in Fig. 2. The calculated value of E_a is higher than the corresponding average values for E_N and E_G. The value of E_a can be calculated from the half-time ($t_{0.50}$) values, and

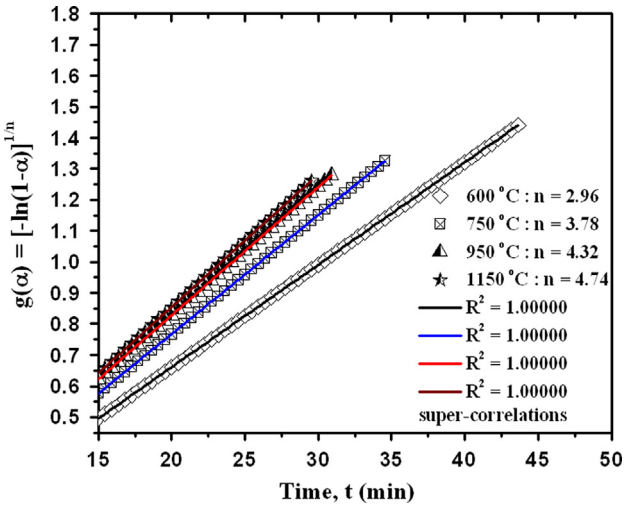

Fig. 6. The linear dependence of $g(\alpha)=[-\ln(1-\alpha)]^{1/n}$ against t, for $n=2.96$, 3.78, 4.32 and 4.74 at $T=600$, 750, 950, and 1150 °C.

Table 5
Summary of calculated half-time ($t_{0.50}$), experimental half-time ($t^*_{0.50}$), the reciprocal half-time ($t^{-1}_{0.50}$), the maximum time (t_{max}) (which corresponds to the inflection point of α–t curve) and the ratio $t_{max}/t_{0.50}$, at the different operating temperatures ($T=600$ °C, 750 °C, 950 °C and 1150 °C).

T (°C)	$t_{0.50}$ (min)	$t^*_{0.50}$ (min)	$t^{-1}_{0.50}$ (min^{-1})	t_{max} (min)	$t_{max}/t_{0.50}$
600	26.749	26.658	0.03738	26.339	0.985
750	23.660	23.256	0.04227	24.033	1.016
950	22.201	21.995	0.04504	22.737	1.024
1150	21.665	21.116	0.04615	22.267	1.028

the derived value can then be compared with the value obtained on the basis of the direct Arrhenius dependence.

4.8. Results of the behavior of $t_{0.50}$ and t_{max} terms

Half-time analysis and linear least squares analysis should yield consistent results and allow one to quantify isothermal rates of crystallization via the generalized Avrami equation. The $t_{0.50}$ and t_{max} represent the important parameters for consideration of the entire decomposition process of zinc ferrite from neutral leach residues, under isothermal experimental conditions. It can be pointed out, that the *half-time parameter* ($t_{0.50}$) can be obtained in two ways: (a) determined for each of the operating temperature, directly from the experimental α–t curves (designated by $t^*_{0.50}$), and (b) using the Avrami rate constant values, from Eq. (13).

Table 5 lists the values of $t_{0.50}$, $t^*_{0.50}$ (the experimental data) $t^{-1}_{0.50}$ (the reciprocal half-time), t_{max} and $t_{max}/t_{0.50}$, at the different operating temperatures (600 °C, 750 °C, 950 °C and 1150 °C) for the investigated decomposition process.

It can be seen from Table 5, that the half-time ($t_{0.50}$) (also and $t^*_{0.50}$) is greater than t_{max} when $n<3.26$ (only in this case, the ratio $t_{max}/t_{0.50}$ is *less than unity* (Table 5)), and $t_{0.50}$ occurs prior to the inflection point of α–t curve when $n>3.26$, but differences between $t_{0.50}$ and t_{max} could be difficult to resolve for reasonable values of n between 3.00 and 4.00. Namely, the half-time ($t_{0.50}$) is coincident with the inflection point of α–t curve, only in the case of *perfect symmetry*, realized on the true determined value, which is $n=3.26$ (this corresponds to the *symmetrically* centered *Gaussian distribution*) [35], and which implies that $t_{0.50}=t_{max}$. Given that at the operating temperatures above 600 °C, the value of n is greater than 3.26 (Tables 1 and 4), then we can clearly see that the $t_{max}>t_{0.50}$ (and the ratio $t_{max}/t_{0.50}>1$) (Table 5).

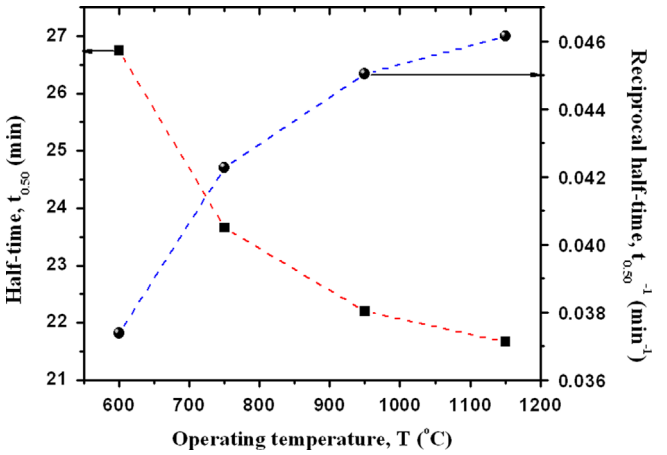

Fig. 7. The trends of half-time ($t_{0.50}$) and the reciprocal half-time ($t^{-1}_{0.50}$) value, as a function of the operating temperature (T), for the isothermal decomposition process of zinc ferrite from neutral leach residues.

4.9. Crystallization rate

It should be noted that the larger half-time indicates a slower crystallization rate (the growth rate (U) can be approximated by $t^{-1}_{0.50}$ (Table 5) i.e., $U\sim t^{-1}_{0.50}$ [36]). Fig. 7 shows the trends of half-time ($t_{0.50}$) and the reciprocal half-time ($t^{-1}_{0.50}$) (the crystal growth rate (U)) as a function of the operating temperature.

The behavior of $t_{0.50}$ and $t^{-1}_{0.50}$ with increasing of the operating temperature corresponds to the same class of the mathematical functions, which is really a class of the exponential functions. However, this dependence *does not belong to the same category* of the exponential functions. In the first case (for dependence of $t_{0.50}$ on T), we have the appearance of the *exponential decay* function of the first order (I), in the following form:

$$t_{0.50}=(t_{0.50})^*+\varepsilon\exp\left(-\frac{T}{T_d{}^*}\right), \tag{23}$$

where $(t_{0.50})^*=21.471$ min, $\varepsilon=171.353$, and $T^*_d=172.37$ °C (Fit status $\equiv R^2=0.99965$ (succeeded fitting $>99\%$)). On the other hand, in the second case (for dependence of $t^{-1}_{0.50}$ on T), we have the appearance of the *exponential growth* function of the first order (I), in the following form:

$$t^{-1}_{0.50}=(t^{-1}_{0.50})^{**}+\varepsilon^*\exp\left(\frac{T}{T_g{}^*}\right), \tag{24}$$

where $(t^{-1}_{0.50})^{**}=0.04678$ min^{-1}, $\varepsilon^*=-0.17426$, and $T^*_g=-205.46$ °C (Fit status $\equiv R^2=0.99992$ (succeeded fitting equal to 100%)). We can see that at the highest operating temperature ($T=1150$ °C), the highest possible crystallization rate for the investigated process is achieved. Also, at the mentioned operating temperature, the rate of formation of the crystal grains is the largest.

Additionally, the *apparent* activation energy ($E^{0.50}_a$) and the *apparent pre-exponential factor* ($k^{0.50}_o$) for the whole decomposition process can also be obtained from the linear dependence $\ln(t^{-1}_{0.50})=\ln k^{0.50}_o-E^{0.50}_a/RT$. The *apparent* activation energy ($E^{0.50}_a$) was calculated, and this value is equal to $E^{0.50}_a=4.0\pm0.9$ kJ mol^{-1}, while the *apparent pre-exponential factor* ($k^{0.50}_o$) was calculated with the value of $k^{0.50}_o=0.0655$ min^{-1}. These values are in good agreement with the values that were obtained from the dependence $\ln(K_A)$ against $1/T$ ($E_a=4.8\pm1.9$ kJ mol^{-1} and $k_o=0.0656$ min^{-1}). Also, these *apparent* activation energy results demonstrate the fact that both approaches can be utilized to determine the *apparent* activation energy (E_a) for the decomposition process of zinc ferrite from neutral leach residues.

Table 6
The thermodynamic functions $\Delta S^{\neq}$, $\Delta H^{\neq}$ and $\Delta G^{\neq}$, for the decomposition process of zinc ferrite from neutral leach residues, at the different operating temperatures (T=600 °C, 750 °C, 950 °C and 1150 °C).

Operating temperature, T (°C)	$\Delta S^{\neq}$ (J K^{-1} mol^{-1})	$\Delta H^{\neq}$ (J mol^{-1})	$\Delta G^{\neq}$ (J mol^{-1})
600	−318.849	−2459.452	275946.741
750	−320.167	−3706.552	323875.516
950	−321.652	−5369.352	388062.508
1150	−322.911	−7032.152	452521.867

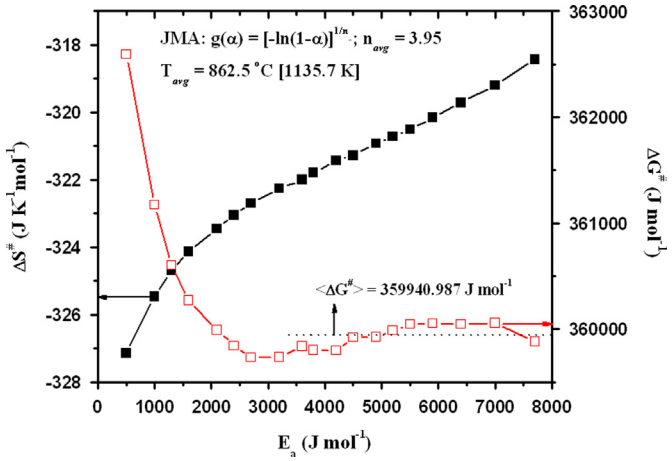

Fig. 8. The dependences of $\Delta S^{\neq}$ and $\Delta G^{\neq}$ values on the effective apparent activation energy (E_a) values, for the JMA kinetic model with the average value of the Avrami constant n_{avg}=3.95, and for the average value of the operating temperature, T_{avg}=862.5 °C [=1135.7 K]; in the same figure, the average value of $\langle\Delta G^{\neq}\rangle$ was also presented. (For interpretation of the references to color in this figure legend, the reader is referred to the web version of this article.)

4.10. Results of thermodynamic analysis

After determination the most probable kinetic mechanism of considered process, we have been calculated the corresponding changes of thermodynamic functions ($\Delta S^{\neq}$, $\Delta H^{\neq}$ and $\Delta G^{\neq}$) with a change in the operating temperature, using the selected thermodynamic equations. Table 6 presents the values of $\Delta S^{\neq}$, $\Delta H^{\neq}$ and $\Delta G^{\neq}$ functions, at the different operating temperatures.

Fig. 8 shows the variations of $\Delta S^{\neq}$ (–■– symbol) and $\Delta G^{\neq}$ (red color –□– symbol) values, with a change in E_a values, for the JMA kinetic model attached to the average value of the Avrami constant n_{avg}=3.95, and for the average value of the operating temperature, T_{avg}=862.5 °C.

With increasing of E_a, $\Delta S^{\neq}$ values increase in progressive trend, but remain only the negative values. On the other hand, the increase in E_a values, leads to a reduction in the value of $\Delta G^{\neq}$, but after about E_a=3200 J mol^{-1} (Fig. 8), $\Delta G^{\neq}$ shows no significant variation with E_a and also shows a tendency to stabilize around the value of $\langle\Delta G^{\neq}\rangle$=359940.987 J mol^{-1}, expressed as the average value (Fig. 8).

5. Discussion

- It can be seen from Fig. 2, that the apparent activation energy varies in the range of 0.5–7.7 kJ mol^{-1}, so that on the basis of the shape of $E_a-\alpha$ curve, we can conclude that the investigated decomposition process takes place through the parallel competing reactions, which have different contributions to the overall process [33]. If we assume that the decomposition process of such a complex system could take place through the model of nucleation and growth of new phases, the above illustrated variations of E_a on α could indicate on the alternated behavior of the Avrami constant (n), starting from the lower range of the operating temperatures (ΔT=600–750 °C) to a higher range of the operating temperatures (ΔT=950–1150 °C). This behavior of the Avrami constant can change the spatial dimensionality of the resulting products of the investigated process.
- The values of the Avrami constant (n) depend on the operating temperature for considered zinc ferrite system (Table 1). At the lowest operating temperature (600 °C), the n value is very close to n=3.00 (~2.96 (Table 1)), while at a higher operating temperature (750 °C), the n value increases to around n=4.00 (~3.78 (Table 1)). However, at the highest operating temperatures (including here the operating temperatures of 950 and 1150 °C), the n values exceeding n=4.00, which achieves the highest value of n=4.74 at 1150 °C (Table 1). Normally, n should not exceed 4 (i.e. the value for three-dimensional bulk nucleation). In the latter case, it can be assumed that the surface induced abnormal grain growth expected for Fe crystallization compounds [37] is responsible for the high value of n for advanced crystallization at high operating temperatures ($T\geq$950 °C). In the case of operating temperature of 600 °C, for which we have the value of n=2.96 ($\approx$3.00) (Table 1), we can expect that the two-dimensional (2D) crystallization mechanism with a disc growth exists. The Avrami constant of n=3.00 implies that the main crystallization mechanism is interface-controlled three-dimensional isotropic growth and early nucleation-site saturation [21]. At the elevated operating temperature of 750 °C, where the value of n=3.78 was identified, the investigated process proceeds through the three-dimensional (3D) crystallization mechanism, with a sphere morphological units [21]. In fact, the transformation for which $3<n<4$ (Table 1) is considered to imply that the process is interface-controlled with a decreasing nucleation rate. On the other hand, an increasing nucleation rate with time can result in the value of $n>4$ [21,38], as can be clearly seen for our investigated system at operating temperatures of 950 and 1150 °C (Table 1).
- From Table 2 we can see that an increase in operating temperature leads to changes in the dimensionality (d) and the nucleation index (m) values, where apparently there is a change in the nucleation mechanism, as well as in the nucleation rate behavior. This is also reflected through the character of the nucleation index (m), which maintains a zero value and the negative value at the operating temperatures of 600 °C and 750 °C, and then becomes positive above 750 °C. It should be noted that the operating temperature range, which is responsible for this change in the crystallization mechanism, is located above the value of 750 °C ($T>$750 °C). Based on the average values of d and m (Table 2), we can conclude that the dominant crystallization mechanism (over the entire observed T range) is the sporadic nucleation with a three-dimensional (3D) sphere growth of new phases.
- It can be observed from Table 3, that on all operation temperatures, the contributions of E_G and E_N to the *effective* activation energy (E_a) are exactly the fractional. It can be seen that an increase in operating temperature causes an increase in fractional values of E_G, while at the same time there is a decrease in fractional values of E_N. This behavior of E_G and E_N in E_a for the overall investigated process, may indicate *secondary nucleation and growth* processes, especially at the lower super-saturation (this state can occurs in the presence of a foreign substrate, which can lead to a decline in the surface free energy (σ), and therefore lead to a reduction of r^* (critical nuclei radius) and ΔG^* (the Gibbs free energy of formation of a nucleus of critical size) values [39], making nucleation more favorable). We can assume that in our case, the probability for the occurrence of this phenomenon increases with increasing of the operating temperature (Table 3).

- Based on the results of the local Avrami constant behavior, for $T=600$ °C, the value of $n(\alpha)$ decreases (from very high values that $n(\alpha)=10.32$) with the fraction of transformation between 0.05 (5%) and 0.70 (70%), and stabilizes after the fraction of transformation exceeds 0.70 (70%). This behavior indicates that the crystallization process is mainly governed by two-dimensional growth [21], where the high value of $n(\alpha)$ at the initial stage indicates, that the nucleation and consequently growth (in two dimensions) process begins (thereby causing that $n(\alpha)$ has a fairly high value). With the progress of crystallization, the $n(\alpha)$ decreases and approaches the value of approximately $n(\alpha)=3.00$ (the value of $n(\alpha)$ in a steady-state condition is marked with a *blue* $n_{steady}=2.60$ in Fig. 3). Decrease of $n(\alpha)$ values shows decrease of the increasing rate of nucleation, which may be attributed to the nucleation saturation. In this stage, two-dimensional growth of crystalline nuclei dominates, and the value of local Avrami constant tends to 3.00 [40]. According to theory of solid-state kinetics, if nucleation sites are small enough, the controlling mechanism must be the interface reaction because of the limited area of the interface, and because the distance over which the diffusion is necessary tends to zero [41]. However, when the particles grow sufficiently, diffusion becomes the limiting factor. The interface-controlled growth model, in steady-state conditions gives the Avrami constant equal to 3.00. At higher operating temperatures, above 600 °C, the variation of $n(\alpha)$ values with the fraction of transformation (α) in the initial stage, has the same form as the variation of $n(\alpha)$ values at $T=600$ °C. However, in these cases, the local Avrami constant reaches the steady-state for the value, which is higher than $n=3.00$ (Fig. 3). At the operating temperature of 750 °C, between 0.55 (55%) and 0.90 (90%), the $n(\alpha)$ is totally stabilized with the value of $n_{steady}=3.40$ (the value of $n(\alpha)$ in a steady-state condition is marked with a *orange* $n_{steady}=3.40$ in Fig. 3). Taking into account the obtained result, we can say that as the crystallization proceeds, the value of n increases (compared to the value of n at the operating temperature of 600 °C) and tends to an average value of about 3.40, indicating that a three-dimensional nucleation and growth process becomes dominating, of which the theoretical value of n should be within 3.00–4.00. We suggest that in this stage of transformation, three-dimensional nucleation and growth of the spherical crystallites inside the bulk of the sample might be occurring.
  At the operating temperatures of 950 and 1150 °C, for the range of the fraction of transformation between 0.60 (60%) and 0.90 (90%), the $n(\alpha)$ values almost coincide in a single value of $n_{steady}=3.97$ (≈ 4.00) (the value of $n(\alpha)$ in a steady-state condition is marked with a *red* $n_{steady}=3.97$ in Fig. 3). The value of $n=4.00$ means that the investigated transformation occurs in a three-dimensional mode with a constant nucleation rate and a constant growth rate [21]. As a general conclusion that can be expressed on the basis of changes in $n(\alpha)$ values with increasing of α, is that the nucleation rate is maximum in the initial stage of the process, and then nucleation rate decreases rapidly followed by growth of the product/products particles.
- In the Region I (Fig. 4) which corresponds to the variation of n values in the range of 2.90–3.38 (in this case we can expect that *in this region there is likely the growth of pre-existing nuclei proceeds parallel with the nucleation process*), appears the change in the values of E_a from 8 to 6 kJ mol^{-1}. Region I belongs to the lower operating temperature region for $T=600$ °C. In the Region II, which corresponds to the medium operating temperature region (for $T=750$ °C), we have a change of n values in the range of 3.38–4.00 (in this case we can expect that *the crystallization proceeds through thermal nucleation and three-dimensional spherical growth*; since in this region the value of n goes to $n=4.00$ (Fig. 4), this means that *the crystallization mechanism is spherule growth from sporadic nucleation, with a reduced nucleation rate* [42]), where the change in the values of E_a from 6 to 3.7 kJ mol^{-1} exists. Finally, in the Region III, belonging to the higher operating temperature region (for $T=950$ and 1150 °C; Fig. 4), the Avrami constant exceeds the value of $n=4.00$, so that changes in the range of 4.07–4.63, and this change in n, corresponding to the changes in the value of E_a from 3.3 to 0.8 kJ mol^{-1}. In the considered region (for Region III in Fig. 4), we suggest the following mechanistic interpretation of the decomposition process at very high temperatures (for $T>950$ °C): having in mind that the value of n in a given region varies over $n=4.00$ (when n exceeds 4.00), the crystallization of probably presented ⟨*amorphous*⟩ phase (which is formed on the observed operating temperatures), should take place in the *autocatalytic stage* of the crystallization process, under the conditions where the rate of nucleation rapidly increases.
  Based on these results, we can conclude that the extremely low value of E_a at the beginning of the decomposition process (at low values of α and for $n>4.00$) (Figs. 2 and 4) is due to the very low effective activation energy needed for the primary crystallites nucleating from the zinc ferrite matrix. In addition, this fact can be confirmed by a significant lowering of the energy barrier for nucleation (which is reflected in the small values of E_N ($\langle E_N\rangle=3.9$ kJ mol^{-1})), compared to the same for the growth ($\langle E_G\rangle=4.4$ kJ mol^{-1}). The high nucleation rate can be attributed to the formation of both Zn and Fe rich regions which provide a high number of heterogeneous nucleation sites, especially for the crystallization process at the high operating temperatures.
- From Fig. 7 we cannot see the emergence of a minimum in $t_{0.50}$ at a given value of T, which lay between the glass transition temperature (T_g) (if we considered the cases for *metal* compounds) and melting temperature (T_m), where they formed the so-called *bell-shaped* curve of the isothermal crystallization. Namely, for example, the extraction of ZnO (followed by zinc extraction in hydrometallurgical processing) is usually carried out below the melting points of the sulfides and oxides involved, usually below the operating temperature of 1200 °C (for example, for willemite (Zn_2SiO_4) the melting temperature is $T_m=1512$ °C, while for hematite (Fe_2O_3), T_m is equal to 1566 °C). On the other hand, in order for the reactions to occur with a sufficient velocity, the operating temperature has to be above 500–600 °C [43]. Thus, the operating temperature range of interest is between 500 °C and 1200 °C.

5.1. Discussion of mechanistic patterns

Based on the established results, the rather low values of the kinetic parameters may indicate on the occurrence of the autocatalytic mechanism at the elevated operating temperatures, where we can observe a very fast nucleation, in the study of such complex decomposition process.

One of the main products of decomposition process of zinc ferrite from neutral leach residues at the elevated temperatures, is the zincite (ZnO) [44,45], which can be further, transformed by smelting process into the zinc. The above process may include the gas–solid reactions at the elevated operating temperatures, which precedes smelting in pyrometallurgy and leaching in hydrometallurgy. For our tested process, we can assume the following system of parallel reactions, which proceed in the respective operating temperature regions, according to the following scheme:

(A) The first expectation operating temperature region belongs to the 400–650 °C, in which the reaction takes place:

$$Fe_2O_{3\,(s)} \rightarrow 2Fe_3O_{4\,(s)} + 1/2O_{2\,(g)}. \quad (25)$$

It was found that the reduction of hematite to magnetite [46,47] may be accompanied by the formation and growth of nuclei model or the phase-boundary reaction model,

respectively, depending on the operating temperature range [48–51]. The X-ray diffraction (XRD) investigations [48,49] showed the dependence of reduction route on the operating temperature are as the following:

$$Fe_2O_3 \rightarrow Fe_3O_4 \rightarrow Fe, \text{ for } T < 450\ ^oC \quad (25a)$$

$$Fe_2O_3 \rightarrow Fe_3O_4 \rightarrow Fe_xO + Fe \rightarrow Fe, \text{ for } 450\ ^oC < T < 570\ ^oC \quad (25b)$$

$$Fe_2O_3 \rightarrow Fe_3O_4 \rightarrow FeO \rightarrow Fe, \text{ for } T > 570\ ^oC. \quad (25c)$$

Given the physical nature of the original sample, and the chemical composition of the final decomposed materials, we will take a look at a general chemical equation, which is represented by Eq. (25). It should be noted that the range of operating temperatures that are used, as well as the partial pressure of oxygen can strongly affect on the reductiuon rate in Eq. (25). It has been shown that the relatively low operating temperature (450–600 °C), and rather high partial pressures of oxygen (O_2) significantly accelerate the transformation of Fe_2O_3 into Fe_3O_4 (Fe^{2+} becomes much more stable in relation to Fe^{3+} at decreasing of partial pressure of O_2) [52,53]. We believe that the operating temperature of 600 °C is ideal for the transformation that takes place by the reaction in Eq. (25). In fact, no matter what the process in Eq. (25) takes place in a system of several parallel reactions, we believe if it came to a complete formation of metallic iron, from wüstite (FeO) transformation, in that case it would probably show a greater variation (by means of *amplitude of variation*) of E_a with α (in the sense of certain *decrease* in the value of E_a, at a certain value of α). Such behavior is not observed in Fig. 2. It was shown, that in the kinetic study of Fe_2O_3 reduction process, in the T range from 300 to 740 °C, the gradual decrease of E_a values can be detected [54]. Specifically, this decline in the E_a values becomes greater with increasing of α in the final stage of the reduction process beyond $\alpha = 0.80$ [54]. One of the reasons for this behavior is just the transformation of FeO during reduction process.

In the considered case, we can assume that at the operating temperature of $T = 600$ °C, the reduction reaction of Fe_2O_3 into Fe_3O_4 is fairly fast (characterized by the steadily increasing of the nucleation rate) and seriously influenced by the percentage of oxygen deposition and external mass transfer, during the two-dimensional growth of magnetite nuclei into uniformly circular discs [55]. This mechanism suggests that the reduction process at the considered operating temperature is controlled by interface-controlled kinetic model. Namely, according to the above mechanism, we can assume that in this case, we can expect that the magnetite initially forms as a surface layer on the hematite reactant, and then the gradually replaces the hematite. Nucleation of magnetite appears to be a highly favored process, as is attested by the rapid initial rate at which the hematite reduction takes place (this is confirmed by the results presented in Tables 1 and 4 for $T = 600$ °C). Further, it can be assumed that the reduction process is probably initiated by hematite reaction with the carbon, which was present in the initial tested sample. It can be pointed out, that the reduction of hematite to magnetite is frequently accompanied by the formation of pores, which are preserved during subsequent reduction to wüstite (Eq. (25c)) [56]. The size and distribution of these pores change with an operating temperature that was used. In this sense, the temperature conditions under which the magnetite is formed can play a vital role in the entire process.

(B) The second expectation operating temperature region belongs to the 700–950 °C for willemite decomposition process:

$$Zn_2SiO_4 \rightarrow Zn^o{}_{(g)} + SiO_2 + O_2. \quad (26)$$

The classical formula for zinc silicate is 2ZnO* SiO_2 [57]. It can be seen as a mixture of zinc oxide and silicon dioxide. As a consequence, the interpretation of the course of the decomposition can be divided into two reaction steps:

$$Zn_2SiO_4 \rightarrow 2ZnO + SiO_2 \text{ (first reaction step)} \quad (26a)$$

$$ZnO \rightarrow Zn^o + 1/2O_2 \text{ (second reaction step)} \quad (26b)$$

Thermo-analytical studies reveal that the rate of the decomposition reaction is the same as the dissociation of pure ZnO [58]. The liberation of ZnO from the silicate seams not to be the rate limiting step [59]. If we consider Eq. (26a) (through the obtained kinetic results), the formation of ZnO from willemite transformation proceeds by the process which is controlled by the nucleation, and having the spherical structures. Namely, the zincite (ZnO) crystallization process probably occurs through the polyhedral crystal growth [60] mechanism (i.e., three-dimensional growth), where the value of n approaches to $n = 4.00$. The second reaction step (described by Eq. (26b)) occurs when incurred ZnO probably left a small open area between the Zn_2SiO_4 shell and the ZnO core. The vacuum in this open area facilitated the decomposition of the rest of zincite core to yield the Zn vapor and O_2 vapor at the operating temperatures above 800 °C ($\approx$800–900 °C). We believe that in this case, the Zn_2SiO_4 shell is not thin enough, so that the evolution of gaseous zinc and oxygen are not limited by diffusion through a solid matrix. It has to be kept in mind that ZnO decomposes into the elements below the melting point ($T_m^{ZnO} = 1975$ °C) if the oxygen partial pressure is too low. This is important for the deposition of such type of oxides at the higher substrate operating temperatures. Namely, the vapor pressure of ZnO is high already at about 1400 °C, which makes it difficult to grow single crystals from its own melt. The stoichiometric width of ZnO below 600 °C is rather narrow. For temperatures higher than 600 °C, Hagemark and Toren [61] measured the Zn–$Zn_{1+x}O$ phase boundary by an electro-chemical method, and conductivity measurements assuming that excess zinc constitutes a shallow donor in ZnO. The new measurements performed by Tomlins et al. [62] suggest that Hagemark and Toren actually measured the phase boundary Zn–ZnO_{1-x} i.e., the concentration of *oxygen vacancies*. In that case, the oxygen vacancies can be generated in ZnO during crystallization. As a result, ZnO grew slightly faster and formed more rounded (in terms of surfaces) polyhedral structures.

(C) The expected temperature range for anglesite ($PbSO_4$) decomposition is the 750 °C < T < 950 (~980) °C [63], and the process can be presented in the form of the following equation:

$$PbSO_{4\ (s)} \rightarrow PbO_{(s)} + SO_2 + 1/2O_2. \quad (27)$$

Based on the established results, we can assume that in this case, probably exists a three-dimensional growth of the formed PbO particles, where the nucleation rate, after a certain time period, tends to reach a constant value. The exposed assumption is a typical for the case of obtaining of the large crystals, in the form of long and laminar structure [63].

(D) The final production of zinc oxide (ZnO) is surely completed at the operating temperature of 1200 °C, so that we can

introduce the following reaction in the form:

$$3ZnO \cdot Fe_2O_3 \rightarrow 3ZnO + 2Fe_3O_4 + 1/2O_2 \text{ (for } T > 1000\ ^{o}C). \quad (28)$$

The catalytic complex of $ZnO \cdot Fe_2O_3$ is split at the very high operating temperatures (for $T > 1000\ ^{\circ}C$) in a non-complex form as $ZnO + Fe_3O_4 + 1/2O_2$. The complex $ZnO \cdot Fe_2O_3$ likely to be autocatalytic decomposed into ZnO and other chemical species, which significantly reduces the energy barrier for a given process. In the case of autocatalytic reaction, the reaction rate is strongly influenced by the concentration of the formed product. In the considered decomposition process, the overall decomposition reaction rate is strongly depends on the amount of the obtained zincite (ZnO).

It can be pointed out, that the rate of investigated process increases, when the nucleation process is autocatalytic, causing an increase in the value of the Avrami constant above $n=4.00$ ($n > 4.00$) [64]. From the obtained results, we may conclude that the process which occurs at the operating temperatures $T \geq 950\ ^{\circ}C$ surely proceeds through the autocatalytic reaction mechanism (Tables 1, 2 and 4). This result indicates that the rate of nucleation abruptly increases, at a very early stage of the observed process.

Based on very high value of the Avrami constant, especially at $T=1150\ ^{\circ}C$ ($n=4.74$, Table 1), we can expect the effect of branching, especially in response to the initial compound that has autocatalytic properties (Eq. (28)). In this case, we will have an extremely low value of E_a (Fig. 4). The formation of the branches is the nucleation of new crystals on the columnar facets of ZnO crystals. One might expect the existence of the line defects under the branched crystals. These line defects that are created, serve as the pin-points for the secondary nucleation to occur. Branch growth on the single crystalline ZnO further supports the idea that the new crystals are mostly formed on the defect sites, such as edges or holes. Also, it should be noted that the increase in the operating temperature in Zn vapor did not result in a decrease of the existing in Zn vacancies [65]. If Zn interstitials had diffused into the crystal, then one would have expected the open-volume *defects* to have been filled. Instead, the Zn vapor may cause an increasing in O vacancies in the bulk by growing new ZnO on the surface. At this point, we should say that it was found, that the zinc pressure (through the vapor transport) can act auto-catalytically inducing O_2 and Zn partial pressures higher than the equilibrium ones, and promoting the decomposition process [66].

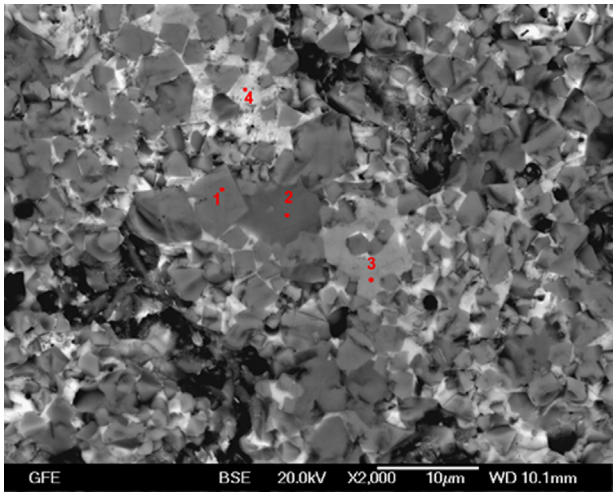

Fig. 9. The SEM image of the final representative sample after the thermal decomposition process, at the operating temperature of $T=1150\ ^{\circ}C$.

After completion of the thermal decomposition process of the investigated sample, it was observed the presence of particles with different forms and sizes in a final structure. The corresponding SEM image of the final representative sample after the thermal decomposition at the operating temperature of $T=1150\ ^{\circ}C$, is shown in Fig. 9.

Fig. 9 clearly shows the existence of specific areas containing the four different particle types. According to the obtained particle shapes, we can quite confidently assume that we have a strong presence of zinc after the thermal decomposition (area "1" in Fig. 9), which indicates that there has not been intense evaporation. The area "1" shown in Fig. 9 is the dominant one. The second important area (area "2" in Fig. 9) can be attributed to the magnetite (Fe_3O_4) structure (namely, the iron is present only in the form of Fe_3O_4, and the final product, which underwent decomposition, has the *magnetic properties* [67–70] as the opposed to the original material [1]; it can be pointed out that the mixed ferrites posses more strongly expressed magnetic properties than those of the individual ferrites – the maximum magnetic interaction in these ferrites was observed at the different zinc contents [71,72]). The remaining two areas in Fig. 9 (areas "3" and "4", which are much less dominant (some brighter parts in Fig. 9)), can be attributed to the remains of magnesium in the form of $Mg_2Si_2O_6$ and the possible presence of lead oxide particles, which was confirmed in our previous paper, using the energy disperse spectroscopy (EDS) [1].

For explanation a thermo-chemical prediction of the formed products, the FactSage® thermo-chemical software was used, and this is represented in Fig. 10.

The bold color lines (Fig. 10) are related to the mass changes for the investigated decomposition process. It is strictly depend on the amount of nitrogen, with enough amount of nitrogen as a carrier gas. It can be seen that is the thermodynamically possible to decompose the ferrite, where the iron contents changed to the magnetite, Fe_3O_4 (the full thin line in Fig. 10). The highest possibility has the formation of Fe_3O_4, which is compatible to the phase stability in the diagram for the system Zn–Fe–S–O [1].

5.2. Discussion of thermodynamic studies

Table 6 shows that the entropy of activation ($\Delta S^{\neq}$) has a negative value at all of the observed operating temperatures, indicating that the corresponding activated complexes had higher degrees of arrangement compared to their initial states. The negative value of the enthalpy of activation ($\Delta H^{\neq}$) identified at all operating temperatures, suggests that the decomposition process is exothermic in nature. Furthermore, the positive value of $\Delta G^{\neq}$ (Table 6) shows that the decomposition process depends on the introduction of heat, and it is a non-spontaneous process. The thermodynamic function $\Delta G^{\neq}$ indicates a non-spontaneous process of decomposition of zinc ferrite from neutral leach residues, at the investigated operating temperatures. This was expected since the ferrite system has been submitted to a forced decomposition and volatilization reactions, caused by the static/isothermal conditions, in a tubular furnace within thermo-analytical measurements. In addition, from results presented in Table 6, we can see that the decomposition process was significantly affected by operating temperature and decomposition can proceed faster for the high values of T.

The results presented in Fig. 8 strongly support the results shown in Table 6, as well as the thermodynamic consideration of the investigated process, which had previously been exposed. However, based on the above presented results, we can assume that the reaction expressed by Eq. (28) should be more thermodynamically favorable, than the willemite decomposition reaction (Eq. (26)). Namely, ZnO and Fe_3O_4 can be found together in the

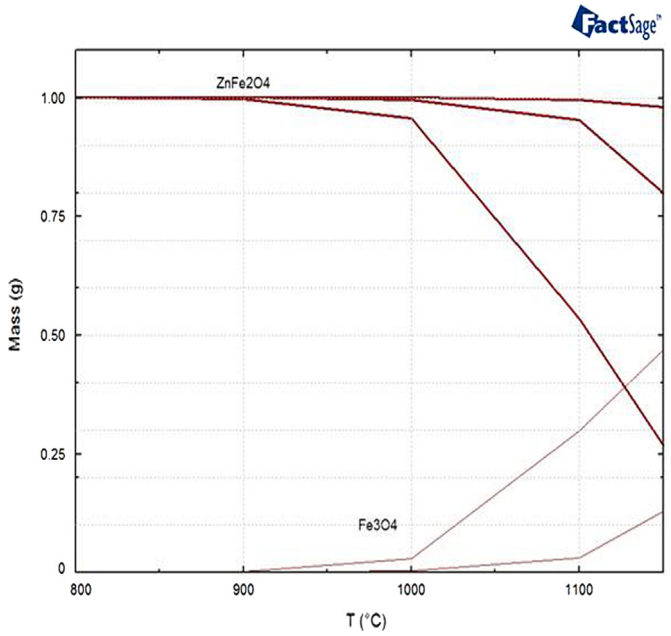

Fig. 10. Predicted product's (using the FactSage® thermo-chemical software) within the investigated operating temperature range during the thermal decomposition process of zinc-ferrite, from the neutral leach residues. (For interpretation of the references to color in this figure legend, the reader is referred to the web version of this article.)

final products of decomposition (along with secondary presented products), when the system is exposed to the very high operating temperatures. In industrial practice, the maximum zinc extraction should be achieved where the activity of $ZnFe_2O_4$ is lowered enough to cause $\Delta G^{\neq}$ to equal zero for a given operating temperature. This is important both from a theoretical and practical point of view, in order to construct a diagram Zn (extraction) – temperature – additives, comparing the theoretical maximum extractions from these activity and thermodynamic calculations with the corresponding surface models, and also for design of conducted experiments [73].

6. Conclusions

The present study is focused on application of the stochastic geometric model in investigation of the decomposition process of zinc ferrite from neutral leach residues, at the different operating temperatures (T=600 °C, 750 °C, 950 °C and 1150 °C). The presented research was supported by the appropriate thermodynamic analysis. The application of this approach on the current decomposition process, has led to the following conclusions:

- Solid state phase transformation kinetics is demonstrated that the observed decomposition represent the complex process, which includes a set of parallel reactions, which occur at the different operating temperature ranges. This fact has been confirmed by varying the Avrami constant (n) with operating temperature, which at higher T exceeds the value n=4.00.
- Based on the calculated average values of dimensionality and nucleation indexes, it was concluded that the dominant crystallization mechanism is the sporadic nucleation, with a three-dimensional (3D) sphere growth of new phases.
- It was found that the contributions of the activation energies for nucleation (E_N) and the growth (E_G), to the apparent (*effective*) activation energy (E_a) of the entire decomposition process, are the exact fractional.
- By varying the local Avrami constant ($n(\alpha)$) with a fraction of transformation (α), it was found that the nucleation rate is *maximum* in the initial stage of the process, and then nucleation rate decreases rapidly followed by the growth of the product particles.
- Based on the dependence of the Avrami constant (n) in a function of the effective activation energy, it was found that at $T>950$ °C, the crystallization process take place in the *autocatalytic* stage, under the conditions where the rate of nucleation rapidly increases. It was established that the high nucleation rate can be attributed to the formation of both Zn and Fe rich regions which provide a high number of heterogeneous nucleation sites.
- It was concluded that based on the behavior of the half-time ($t_{0.50}$) and the reciprocal half-time ($t_{0.50}^{-1}$) values with a change in the operating temperature, the highest possible crystallization rate is achieved at the highest T (1150 °C).
- Thermo-chemical predictions showed that it is possible to carry out the decomposition of ferrite, where the iron contents changed to the magnetite, Fe_3O_4, which is in accordance with the phase stability diagram of Zn–Fe–S–O system.
- Thermodynamic analysis showed that the decomposition process depends on the introduction of heat, and exerts a positive value of the Gibbs free energy of activation. Such a feature was expected since the ferrite system has been submitted to a forced decomposition and volatilization reactions, under isothermal measurements in a tubular furnace.
- The thermo-chemical analysis presented in the current investigation illustrates the formation of Fe_3O_4 phase at the higher temperatures after the decomposition, what can be the usefulness of this study in order to prepare the nanosized magnetic particles.

Acknowledgments

The authors would also like to thank the Ministry of Science and Environmental Protection of Serbia, under the Project 172015 (Bojan Janković).

We like to thank Deutsche Forschungsgemeinschaft DFG in Bonn (Germany) for financial support of the Project FR 1713/13-1: Zn-recovery from steel making dusts – kinetics and mechanism of thermal zinc-ferrite phase decomposition (Srećko Stopić, Aybars Güven and Bernd Friedrich).

References

[1] S. Stopić, B. Friedrich, Kinetics and mechanism of thermal zinc-ferrite phase decomposition, in: Proceeding of EMC 2009, Innsbruck, Austria, 28 June–1 July 2009, pp. 1167–1181.
[2] S. Polsilapa, D.R. Sadedin, N.B. Gray, Treatment of EAF dust and zinc-ferrite thermodynamics and kinetics, in: Proceeding of EMC 2009, Innsbruck, Austria, 28 June–1 July 2009, pp. 1139–1153.
[3] M. Olper, M. Maccagni, From C.Z.O. to zinc cathode without any pre-treatment, the Ezinex process, The Southern African Institute of Mining and Metallurgy, Lead and Zinc, 2008, pp. 85–97.
[4] M. Olper, M. Maccagni, Electrolytic zinc production from crude zinc oxide with the EZINEX® process, in: D.L. Stewart Jr., J.C. Daley, R.L. Stephens (Eds.), Proceedings of the Fourth International Symposium on Recycling of Metals and Engineered Materials, Pittsburgh, Pennsylvania, USA, October 22–25, 2000, pp. 379–396.
[5] M.K. Jha, V. Kumar, R.J. Singh, Review of hydrometallurgical recovery of zinc from industrial wastes, Res. Conserv. Recyc. 33 (2001) 1–22.
[6] T. Havlik, M. Turzakova, S. Stopić, B. Friedrich, Atmospheric leaching of EAF dust with diluted sulphuric acid, Hydrometall. 77 (2007) 41–50.
[7] W. Derda, K. Mierzwa, The thermal treatment of electric arc furnace dust under low gas phase pressure, J. Metall. 48 (2009) 91–94.
[8] D.-G. Zhao, S.-H. Wang, P. Zhao, Thermodynamic of boron oxide reducing with carbothermic method, J. Iron Steel Res. 24 (2012) 19–22.
[9] M.H. Morcali, O. Yucel, A. Aydin, B. Derin, Carbothermic reduction of electric arc furnace dust and calcination of waelz oxide by semi-pilot scale rotary furnace, J. Min. Metall. Sect. B – Metall. 48 (2) (2012) 173–184.

[10] G. Kaupp, F.E. Martinez, H. Ren, V.D. Jaramillo, H. Zoz, High kinetic processing of EAF dust and a new hydrometallurgical recycling scheme, Metallurgy 62 (2008) 819–823.
[11] T. Havlik, S. Stopić, B. Friedrich, Pressure leaching of EAF dust with sulphuric acid, Erzmetall 57 (2004) 113–120.
[12] W.A. Johnson, R.F. Mehl, Reaction kinetics in processes of nucleation and growth, Trans. Am. Inst. Min. Metall. Pet. Eng. 135 (1939) 416–441.
[13] M. Avrami, Kinetics of phase change. I. General theory, J. Chem. Phys. 7 (1939) 1103–1112.
[14] M. Avrami, Kinetics of phase change. II. Transformation–time relations for random distribution of nuclei, J. Chem. Phys. 8 (1940) 212–224.
[15] M. Avrami, Kinetics of phase change. III. Granulation, phase change, and microstructure, J. Chem. Phys. 9 (1941) 177–184.
[16] E.J. Mittemeijer, Review analysis of the kinetics of phase transformations, J. Mater. Sci. 27 (1992) 3977–3987.
[17] J.M. Honig, Thermodynamics: Principles Characterizing Physical and Chemical Processes, third edition, Elsevier Science & Technology Books, Amsterdam, The Netherlands (2007) 1–445.
[18] C.W. Bale, P. Chartrand, S.A. Degterov, G. Eriksson, K. Hack, R. Ben Mahfoud, J. Melançon, A.D. Pelton, S. Petersen, FactSage thermochemical software and databases, Calphad 26 (2) (2002) 189–228.
[19] P. Supaphol, J.E. Spruiell, Isothermal melt- and cold-crystallization kinetics and subsequent melting behavior in syndiotactic polypropylene: a differential scanning calorimetry study, Polymer 42 (2) (2001) 699–712.
[20] B. Wunderlich, Macromolecular Physics, vol. 2, Academic Press, New York, USA (1976) 132–147.
[21] J.W. Christian, The Theory of Transformations in Metals and Alloys, Pergamon Press, Oxford, New York (1965) 53–59.
[22] E.J. Mittemeijer, Fundamentals of Materials Science: The Microstructure–Property Relationship using Metals as Model Systems, Springer-Verlag, Berlin Heidelberg, Germany (2010) 371–497 (chapters 9–10).
[23] H.L. Friedman, Kinetics of thermal degradation of char-forming plastics from thermogravimetry. Application to phenolic plastic, J. Polym. Sci. Part C 6 (1) (1964) 183–195.
[24] W. Xiaofeng, M. Likai, Z. Wei, S. Zhongyuan, S. Yi, Q. Keqiang, Crystallization kinetics of misch metal based bulk metallic glasses, J. Rare Earths 25 (2007) 189–193.
[25] L.A. Belfiore, Crystallization kinetics via spherulitic growth, in: L.A. Belfiore (Ed.), Physical Properties of Macromolecules, first edition,John Wiley & Sons, Inc., Hoboken, New Jersey, USA, 2010, pp. 287–327 (chapter 8).
[26] P. Supaphol, Application of the Avrami, Tobin, Malkin, and Urbanovici–Segal macrokinetic models to isothermal crystallization of syndiotactic polypropylene, Thermochim. Acta 370 (1–2) (2001) 37–48.
[27] X. Weibing, H. Pingsheng, C. Dazhu, Cure behavior of epoxy resin/montmorillonite/imidazole nanocomposite by dynamic torsional vibration method, Eur. Polym. J. 39 (3) (2003) 617–625.
[28] J. Málek, The kinetic analysis of non-isothermal data, Thermochim. Acta 200 (1992) 257–269.
[29] S. Montserrat, J. Málek, P. Colomer, Thermal degradation kinetics of epoxy–anhydride resins: I.: Influence of a silica filler, Thermochim. Acta 313 (1) (1998) 83–95.
[30] E.V. Anslyn, D.A. Dougherty, Transition state theory and related topics in: C. Taylor (Ed.), Modern Physical Organic Chemistry, University Science Books, US, 2006, pp. 365–373.
[31] K. Laidler, C. King, The development of transition-state theory, J. Phys. Chem. 87 (1983) 2657–2664.
[32] S. Vyazovkin, A unified approach to kinetic processing of nonisothermal data, Int. J. Chem. Kinet. 28 (1996) 95–101.
[33] S.V. Vyazovkin, A.I. Lesnikovich, An approach to the solution of the inverse kinetic problem in the case of complex processes: Part 1. Methods employing a series of thermoanalytical curves, Thermochim. Acta 165 (2) (1990) 273–280.
[34] J.R. Macdonald, Thermal activation relations, J. Chem. Phys. 40 (7) (1964) 1792–1805.
[35] D.N.P. Murthy, M. Xie, R. Jiang, Weibull Models, John Wiley & Sons, Inc., Hoboken, New Jersey, USA (2004) 3–16.
[36] J.I. Lauritzen, J.D. Hoffman, Extension of theory of growth of chain-folded polymer crystals to large undercoolings, J. Appl. Phys. 44 (1973) 4340–4352.
[37] R.W. Cahn, P. Haasen, in: R.W. Cahn, P. Haasen (Eds.), Physical Metallurgy, fourth, revised and enhanced edition,North Holland, Amsterdam – Elsevier Science B.V., Amsterdam, The Netherlands, 1996, pp. 135–166.
[38] D. Turnbull, Phase changes, Solid State Phys. Adv. Res. Appl. 3 (1956) 225–306.
[39] D. Kashchiev, G.M. van Rosmalen, Review: nucleation in solutions revisited, Cryst. Res. Technol. 38 (2003) 555–574.
[40] S.E. Offerman, N.H. van Dijk, J. Sietsma, S. Grigull, E.M. Lauridsen, L. Margulies, H.F. Poulsen, M.Th. Rekveldt, S. van der Zwaag, Science 298 (2002) 1002–1005.
[41] J. Burke, The Kinetics of Phase Transformation in Metals, Pergamon Press, Oxford, UK (1965) 191–195.
[42] I.H. Hillier, Modified Avrami equation for the bulk crystallization kinetics of spherulitic polymers, J. Polym. Sci. Part A: Gen. Pap. 3 (9) (1965) 3067–3078.
[43] T. Rosenqvist, Principles of Extractive Metallurgy, second edition, Tapir Academic Press, Trondheim, Norway (2004) 215–223.
[44] A. Moezzi, A.M. McDonagh, M.B. Cortie, Zinc oxide particles: synthesis, properties and applications, Chem. Eng. J. 185–186 (2012) 1–22.
[45] V. Houšková, A. Kalendová, V. Štengl, S. Bakardjieva, Synthesis and properties of morphologically interesting particles of zincite and periclase, J. Phys. Chem. Solids 68 (5–6) (2007) 1198–1202.
[46] A. Matthews, Magnetite formation by the reduction of hematite with iron under hydrothermal conditions, Am. Mineral. 61 (1976) 927–932.
[47] K. Piotrowski, K. Mondal, T. Wiltowski, P. Dydo, G. Rizeg, Topochemical approach of kinetics of the reduction of hematite to wüstite, Chem. Eng. J. 131 (2007) 73–82.
[48] A. Pineau, N. Kanari, I. Gaballah, Kinetics of reduction of iron oxides by H_2 Part I: low temperature reduction of hematite, Thermochim. Acta 447 (2006) 89–100.
[49] A. Pineau, N. Kanari, I. Gaballah, Kinetics of reduction of iron oxides by H_2 Part II. Low temperature reduction of magnetite, Thermochim. Acta 456 (2007) 75–88.
[50] K. Piotrowski, K. Mondal, H. Lorethova, L. Stonawski, T. Szymanski, T. Wiltowski, Effect of gas composition on the kinetics of iron oxide reduction in a hydrogen production process, Int. J. Hydrog. Energy 30 (15) (2005) 1543–1554.
[51] C. Messi, P. Carniti, A. Gervasini, Kinetics of reduction of supported nanoparticles of iron oxide, J. Therm. Anal. Calorim. 91 (2008) 93–100.
[52] R. Hansson, P.C. Hayes, E. Jak, Phase equilibria in the Fe–Zn–O system at conditions relevant to zinc sintering and smelting, in: Proceedings of the VII International Conference on Molten Slags Fluxes and Salts, The South African Institute of Mining and Metallurgy, South Africa, 2004, pp. 209–214.
[53] G. Li, T. Jiang, Y. Zhang, Z. Tang, Recrystallization of Fe_2O_3 during the induration of iron ore oxidation pellets, in: K. Sztwiertnia (Ed.), Recrystallization, InTech Open Science Publishing, Shanghai, China, 2012, pp. 329–350 (chapter 13).
[54] S.-S. Yung, J.-S. Lee, In-situ kinetic study of hydrogen reduction of Fe_2O_3 for the production of Fe nanopowder, Mater. Trans. 50 (9) (2009) 2270–2276.
[55] A. Chakraborty, Kinetics of the reduction of hematite to magnetite near its Curie transition, J. Magn. Magn. Mater. 204 (1–2) (1999) 57–60.
[56] A.V. Bradshaw, A.G. Matyas, Structural changes and kinetics in the gaseous reduction of hematite, Metall. Mater. Trans. B 7 (1) (1976) 81–87.
[57] O. Knacke, O. Kubaschewski, K. Hesselmann, Thermochemical Properties of Inorganic Substances II, second edition, Springer-Verlag, Berlin, Germany (1991) 2336–2348.
[58] R. Swaminathan, J. Woods, S. Calvin, J. Huth, M.E. McHenry, Microstructural evolution model of the sintering behavior and magnetic properties of NiZn ferrite nanoparticles, Adv. Sci. Technol. 45 (2006) 2337–2344.
[59] M. Hursit, O. Laçin, H. Saraç, Dissolution kinetics of smithsonite ore as an alternative zinc source with an organic leach reagent, J. Taiwan Inst. Chem. Eng. 40 (1) (2009) 6–12.
[60] H.J. Fan, Y. Yang, M. Zacharias, ZnO-based ternary oxide nanotubes and nanowires, J. Mater. Chem. 19 (7) (2009) 885–900.
[61] K.I. Hagemark, P.E. Toren, Determination of excess Zn in ZnO-phase boundary Zn–Zn1+XO, J. Electrochem. Soc. 122 (1975) 992–994.
[62] G.W. Tomlins, J.L. Routbort, T.O. Mason, Zinc self-diffusion, electrical properties, and defect structure of undoped, single crystal zinc oxide, J. Appl. Phys. 87 (2000) 117–123.
[63] S.A.A. Sajadi, A comparative investigation of lead sulfate and lead oxide sulfate study of morphology and thermal decomposition, Am. J. Anal. Chem. 2 (2) (2011) 206–211.
[64] A. Gualtieri, P. Norby, G. Artioli, J. Hanson, Kinetic study of hydroxysodalite formation from natural kaolinites by time-resolved synchrotron powder diffraction, Microporous Mater. 9 (3–4) (1997) 189–201.
[65] F.A. Selim, M.H. Weber, D. Solodovnikov, K.G. Lynn, Nature of native defects in ZnO, Phys. Rev. Lett. 99 (8) (2007) 085502.
[66] R. Tena-Zaera, M.C. Martínez-Tomás, S. Hassani, R. Triboulet, V. Muñoz-Sanjosé, Study of the ZnO crystal growth by vapour transport methods, J. Cryst. Growth 270 (3–4) (2004) 711–721.
[67] E. Ranjith Kumar, R. Jayaprakash, M.S. Seehra, T. Prakash, S. Kumar, Effect of α-Fe_2O_3 phase on structural, magnetic and dielectric properties of Mn–Zn ferrite nanoparticles, J. Phys. Chem. Solids 74 (7) (2013) 943–949.
[68] J. Azadmanjiri, Preparation of Mn–Zn ferrite nanoparticles from chemical sol–gel combustion method and the magnetic properties after sintering, J. Non-Cryst. Solids 353 (44–46) (2007) 4170–4173.
[69] S. Woltz, R. Hiergeist, P. Görnert, C. Rüssel, Magnetite nanoparticles prepared by the glass crystallization method and their physical properties, J. Magn. Magn. Mater. 298 (1) (2006) 7–13.
[70] J. Xu, H. Yang, W. Fu, K. Du, Y. Sui, J. Chen, Y. Zeng, M. Li, G. Zou, Preparation and magnetic properties of magnetite nanoparticles by sol–gel method, J. Magn. Magn. Mater. 309 (2) (2007) 307–311.
[71] B.S. Boyanov, Synthesis and Neel temperature determination of ferrites from the $MO-ZnO-Fe_2O_3$ systems (M=Cu, Co and Ni), J. Therm. Anal. Calorim. 41 (6) (1994) 1607–1617.
[72] P. Poddar, H. Srikanth, S.A. Morrison, E.E. Carpenter, Inter-particle interactions and magnetism in manganese–zinc ferrite nanoparticles, J. Magn. Magn. Mater. 288 (2005) 443–451.
[73] P.C. Holloway, T.H. Etsell, Mineralogical transformations in Altasteel electric arc furnace dust roasted with Na_2CO_3 and secondary ferrite-forming additives, J. Miner. Mater. Charact. Eng. 7 (1) (2007) 1–26.